MATERIALS CHEMISTRY
FRONTIERS

RESEARCH ARTICLE

View Article Online
View Journal | View Issue

Cite this: *Mater. Chem. Front.*, 2021, **5**, 4604

Arm modulation of triarylamines to fine-tune the properties of linear D–π–D HTMs for robust higher performance perovskite solar cells†

Heng Zhang,[a] Bingxue Wu,[a] Quanping Wu,*[a] Zhihui Wang,[b] Song Xue[a] and Mao Liang *[a]

Received 2nd February 2021,
Accepted 8th April 2021

DOI: 10.1039/d1qm00190f

rsc.li/frontiers-materials

Most organic hole-transport materials (HTMs) toward efficient perovskite solar cells (PSCs) thus far still rely on methoxytriphenylamine, which limits the photovoltage and decrease the stability of PSCs. However, alternative donors with better performance are scarce. Herein, we employ the synergistic strategy to modulate the properties of triarylamines (TAAs) by introducing different functional groups on their outer/inside arm. It is found that the arm modulation of asymmetrical TAAs can balance well the hole transport, HOMO level, film quality and stability of the studied HTMs M140 and M141. The photovoltaic performances of devices with doped and dopant-free M140 and M141 have been investigated. Encouragingly, the doped M141 device featuring the *N*-(9,9-dimethyl-9*H*-fluoren-2-yl)-*N*-(4-methoxyphenyl)spiro[fluorene-9,9′-xanthen]-2-amine (MP-F-SFX) asymmetrical TAA achieves a significantly boosted power conversion efficiency (PCE) of 20.74%, accompanied by long-term stability in ambient air. This work not only provides a promising donor candidate (MP-F-SFX), but also reveals an effective way of using rationally designed asymmetrical triarylamines to fine-tune the properties of linear D–π–D HTMs.

1. Introduction

Organic–inorganic metal halide perovskite solar cells (PSCs) have gained enormous attention during the past few years because of their excellent optoelectronic properties, low cost and high efficiency, which make them promising candidates for next-generation photovoltaic devices.[1–3] PSCs hold considerable promise in photoelectric energy conversion; their power conversion efficiencies (PCEs) have increased rapidly due to the improvement of perovskite composition, optimization of transport layers, and passivation of interfaces.[4–13] Recently, an enormous amount of effort has been devoted to hole-transport materials (HTMs) for further enhancing the efficiency and stability of halide PSCs.[14–59] HTMs not only efficiently extract holes from the perovskite active layer but also suppress charge recombination at the anode, which makes them a crucial part of state-of-the-art n–i–p-type PSCs.

HTMs can be divided into four main categories: inorganic HTMs, polymers, metal–organic compounds and organic molecular HTMs.[60] In the case of organic HTMs, 2,2′,7,7′-tetrakis(*N*,*N*-di-pmethoxyphenylamino)-9,9′-spirobifluorene (Spiro-OMeTAD) is the most commonly used organic HTM for PSCs, in which record-high efficiencies have been achieved. However, Spiro-OMeTAD suffers from a low hole mobility in its pristine form because of its propeller-like structure due to the sp^3-hybridization atom linkage.[14] In addition, its complex synthetic process significantly limits the suitability for large-scale industrial application of Spiro-OMeTAD in PSCs. Small-molecule alternatives with high hole mobility have been extensively investigated.[60–65] Among them, most of the linear small molecule HTMs contain the core and the methoxy-substituted triphenylamine (OMe-TPA), in which the two methoxy groups are very beneficial for hole transport. However, the methoxy moieties significantly upshift the HOMO level and decrease the glass transition temperature (T_g) of HTMs, which limits the open-circuit voltage (V_{OC}) and reduce the device stability.[49,66,67] In this respect, a balanced point between the advantage of hole transport and the disadvantages of V_{OC} loss and low stability must be determined.

Thanks to their tunable functionalized structures, it is attractive to optimize the properties of HTMs through the design of triarylamines (TAAs), which can be modulated by rational design of their outer and inside arms to obtain HTMs characterized by desired properties. Even though the effectiveness of

[a] *Tianjin Key Laboratory of Organic Solar Cells and Photochemical Conversion, Tianjin Key Laboratory of the Design and Intelligent Control of the Advanced Mechanical System, School of Mechanical Engineering, Tianjin University of Technology, Tianjin 300384, P. R. China. E-mail: liangmao717@126.com, wqping@ustc.edu.cn*
[b] *Jiangsu Provincial Key Laboratory of Palygorskite Science and Applied Technology, College of Chemical Engineering, Huaiyin Institute of Technology, Huaian 223003, Jiangsu Province, P. R. China*

† Electronic supplementary information (ESI) available. See DOI: 10.1039/d1qm00190f

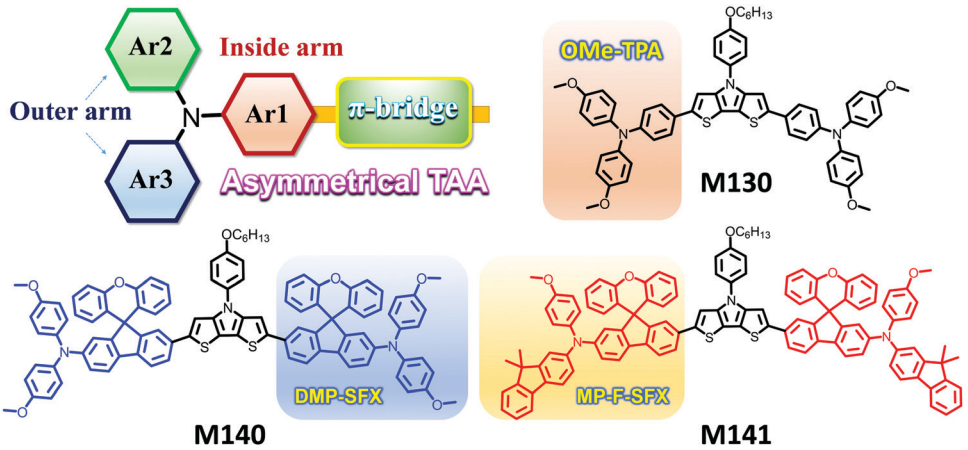

Fig. 1 Chemical structures of asymmetrical TAAs, M140, M141 and M130.

the asymmetrical strategy has been demonstrated in optimizing bis(4-methoxyphenyl)amine for HTMs,[57,66,68–70] asymmetrical TAAs have rarely been reported in linear D–π–D HTMs and the influence of the outer arm and inside arm (Fig. 1) of asymmetrical TAAs on the optoelectronic properties and hole transport of linear D–π–D HTMs remains to be addressed.

Herein, we report two new linear D–π–D HTMs (M140 and M141) based on asymmetrical TAAs, *i.e. N*,*N*-bis(4-methoxyphenyl)-spiro[fluorene-9,9′-xanthen]-2-amine (DMP-SFX, Fig. 1) and *N*-(9,9-dimethyl-9*H*-fluoren-2-yl)-*N*-(4-methoxyphenyl)spiro[fluorene-9,9′-xanthen]-2-amine (MP-F-SFX). To the best of our knowledge, both asymmetrical TAAs have never been evaluated in linear D–π–D HTMs. Breaking the symmetric structure of triphenylamine by replacing the benzene unit with a dimethylfluorene or SFX to form M140/M141 enabled us to deeply understand how the outer and inside arms of TAAs affect the photophysical, electrochemical, and thermal properties and hole mobilities as well as the photovoltaic performance of HTMs.

We demonstrated that the arm modulation of asymmetrical TAAs can balance well the hole transport, HOMO level, film quality and stability of linear D–π–D HTMs. Introducing the SFX unit as the inside arm can effectively downshift the HOMO level of HTMs and thus improve the V_{OC} of devices. On the other hand, the outer arm not only plays an extra role in preventing HTM aggregation, but also shows positive effects on the energy level, hole transport and molecular stability of HTMs. More notably, the synergistic effect due to the inside and outer arms of MP-F-SFX resulted in a doped HTM characterized by significantly reduced V_{OC} loss, improved charge carrier mobility and excellent film formability. Accordingly, the champion cell based on doped M141 with the MP-F-SFX donor achieved a PCE of up to 20.74%. These results qualify MP-F-SFX as a potential challenger to OMe-TPA.

2. Experimental

2.1 Design and synthesis

The rationale for developing asymmetrical TAAs is as follows: (1) we retained at least one methoxy at the arms of TAAs for efficient hole-transport. (2) The fused ring structure of dimethylfluorene/spiro[fluorene-9,9′-xanthene] (SFX) is expected to increase the thermal stability and improve the film quality of HTMs. (3) Dithieno[3,2-*b*:2′,3′-*d*]pyrrole (DTP) was employed as the core to facilitate intramolecular charge transfer (ICT) in D–π–D HTMs. In addition, OMe-TPA-based M130 (Fig. 1) was evaluated as a reference HTM. The synthetic routes towards the target HTMs are shown in Scheme S1 (ESI†). The final molecules were identified using NMR spectra; these analytical data for all HTMs are in good agreement with the formulated structures. Details of measurements, device fabrication, instrumentation, characterization, and ^{1}H NMR and ^{13}C NMR spectra (Fig. S1–S5) of the new compounds are shown in the ESI.†

3. Results and discussion

3.1. Optoelectronic properties and calculation

The optical properties of M140 and M141 were evaluated by using absorption and emission spectroscopy (Fig. 2a), with the corresponding photophysical data summarized in Table 1. In CH_2Cl_2 solution, the UV-vis absorption spectra of M140 and M141 were similar, displaying absorption peaks (λ_{abs}) at 446 and 447 nm, respectively. Clearly, the influence of the peripheral *N*-substituent in the SFX-based triarylamine on the ICT of the HTM is insignificant, which is different from a previous study reported by Seo and co-workers.[66] They observed a 16 nm shift of the absorption peak when the outer anisole was replaced by the fluorene unit in the peripheral group of spiro compounds. Therefore, the influence of the outer arm on the ICT progress depends on the conjugation strength between two nitrogen atoms. In the cases of M140 and M141, their inside arm governs the optical bandgap as well as absorption properties. The λ_{abs} value of M140 has a significant bathochromic shift (21 nm) in comparison with M130 due to an extended π-conjugation through the SFX unit compared to the benzene unit. To gain insight into the structural and electronic properties of both the HTMs, density functional theory (DFT) calculations were performed at the B3LYP/6-31G(d) level (Fig. 2b). The highest occupied molecular orbitals (HOMOs) for M140 and M141 are

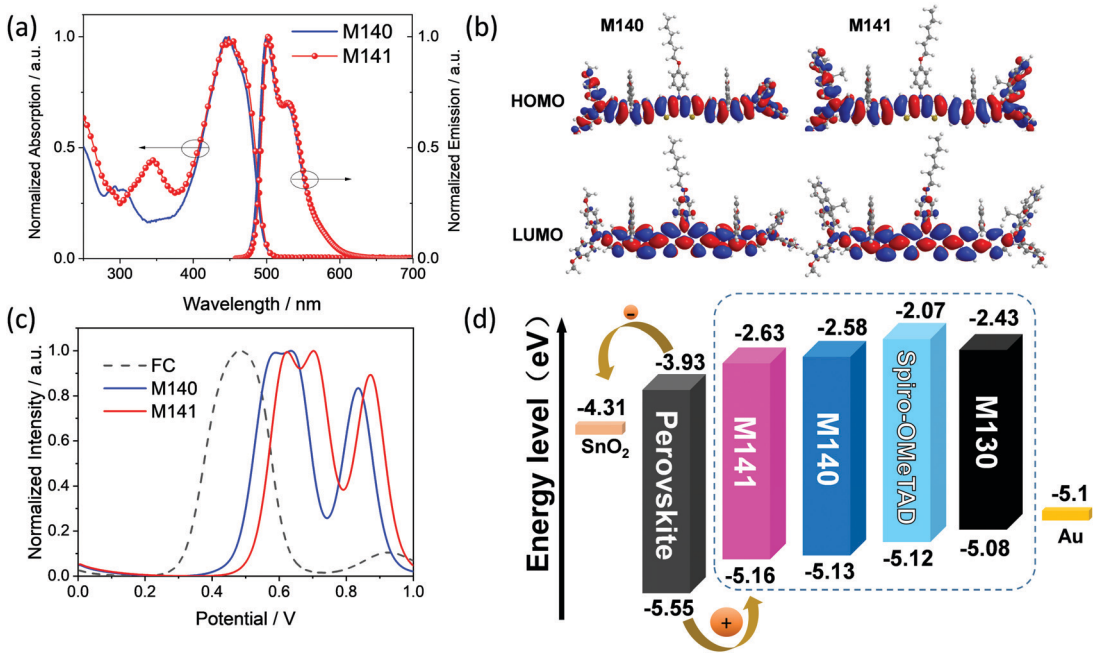

Fig. 2 (a) The UV-vis absorption and emission spectra of HTM solutions. (b) Molecular orbital surfaces of the HOMO and LUMO. (c) DPV curves of HTMs and ferrocene. (d) Energy level diagram of the device.

Table 1 Optical properties, redox potentials, mobilities and T_g of HTMs

HTM	λ_{abs}[a]/nm	E_g[b]/eV	HOMO/V *vs* NHE[c]	LUMO/V *vs* NHE[d]	Mobility/cm^2 V^{-1} s^{-1}	Conductivity/S cm^{-1}	T_g/°C
M140	446	2.55	−5.13	−2.58	2.39×10^{-4}	4.98×10^{-6}	183
M141	447	2.53	−5.16	−2.63	5.60×10^{-4}	5.34×10^{-6}	144
M130[e]	425	2.65	−5.08	−2.43	3.71×10^{-4}	3.70×10^{-6}	101

[a] The absorption peaks of M140 and M141 in DCM. [b] E_g is the energy gap between the HOMO and LUMO. [c] The HOMO was recorded by DPV. [d] The LUMO was calculated from HOMO − E_g. [e] These data have been reported in ref. 36.

localized on the whole molecules, while the electron density distributions of their lowest unoccupied molecular orbitals (LUMOs) are mainly located on the SFX-DTP-SFX part of the HTMs. Therefore, both M140 and M141 have a large degree of conjugation, which is an important approach to improve interchain π–π overlapping while obtaining broader absorption.[71]

To evaluate the band alignment of these HTMs with the perovskite, differential pulse voltammetry (DPV) measurement was carried out (Fig. 2c) and the corresponding data are listed in Table 1. The incorporation of dimethylfluorene in the outer arm of M141 resulted in a low-lying HOMO of −5.16 eV, which is slightly deeper than that of M140 (−5.13 eV). In contrast, the HOMO energy level of M130 (−5.08 eV) was upshifted as compared to that of M140 when the inside arm (SFX) was replaced with the benzene unit. Apparently, the incorporation of bulky groups with weak donating capability either in the inside or outer arm in TAAs is beneficial for down-shift of the HOMO level. On the other hand, the LUMO levels of M140 and M141 are calculated to be −2.58 eV, and −2.63 eV, respectively, which are more positive than that of the mixed-perovskite (−3.93 eV).

3.2. Thermal properties

Fig. 3 displays the differential scanning calorimetry (DSC) thermograms of M140 and M141 after two heating–cooling cycles. Only a T_g was recorded during the second cooling for M140 and M141, with T_g values of 144 °C and 183 °C, respectively, indicating the amorphous properties of both HTMs.[72] Moreover, the T_g values of M140 of M141 are much higher than that of M130 (101 °C, Table 1), suggesting their significantly better morphological stability. Clearly, the T_g values of linear TAA HTMs can be improved by the structural bulk added in the outer and inside arms, leading to higher stability since phase transitions could be avoided during device operation. The decomposition temperatures (T_d) of M140 and M141 were assessed by thermogravimetric analysis (TGA). Both HTMs have a relatively high decomposition temperature around 430 °C, with a weight loss of 5% (Fig. S6, ESI†), indicating their good thermal stability.

3.3. Conductivity and hole mobility of doped HTMs

To investigate the influence of peripheral triarylamines on the final photovoltaic properties of these DTP HTMs, we recorded

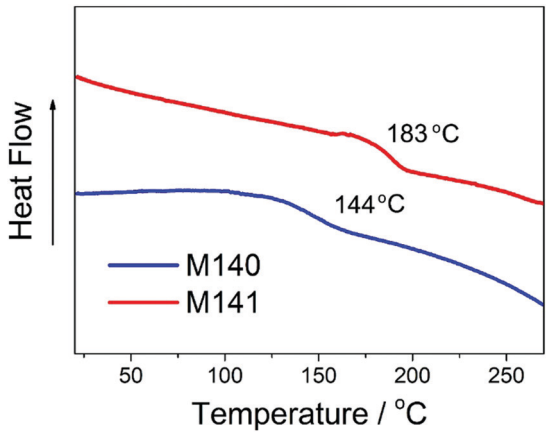

Fig. 3 DSC curves of M140 and M141.

the conductivity and hole mobility of doped M140 and M141. The two-contact electrical conductivity (Fig. 4a) and space-charge-limited currents (SCLCs, Fig. 4b) were analyzed, and the corresponding data are listed in Table 1. The conductivity of M141 (5.34×10^{-6} S cm^{-1}) is slightly higher than that of M140 (4.98×10^{-6} S cm^{-1}), which causes a positive effect on the intermolecular charge transfer. Similarly, the hole mobility of M141 (5.60×10^{-4} cm^2 V^{-1} s^{-1}) is higher than that of M140 (2.39×10^{-4} cm^2 V^{-1} s^{-1}). Recently reports proposed that introduction of 3D electronic structures in HTMs could improve the intermolecular interactions to some extent and thus enhance the transporting channels.[70] Therefore, it is reasonable for M141 to have a higher conductivity and hole mobility than those of M140 because MP-F-SFX is a more twisted triarylamine than DMP-SFX.

3.4. Photovoltaic properties of doped HTMs

The photovoltaic performance of the PSC devices using doped M140 and M141 as HTMs with a device configuration of ITO/SnO_2(with KCl treatment[73])/perovskite/HTL/Au was systematically investigated. Doped M130 and Spiro-OMeTAD based PSCs with the same device configuration were employed as references to better clarify the photovoltaic performance. The incident photon-to-current conversion efficiency (IPCE) was measured as shown in Fig. S7 in the ESI.† Compared with the J_{SC} values from J–V measurements, the integrated currents from the IPCE measurements are slightly lower, a result which can be attributed to the weaker intensities of individual wavelengths.[39]

Fig. 5a displays the cross-sectional scanning electron microscope (SEM) image of a device based on M141. The thicknesses of the M141 and perovskite films are *ca.* 175 and 420 nm, respectively. It can be found that M141 forms a dense film on the flat perovskite-absorbing layer. This can be attributed to the twist structure of MP-F-SFX, which could alleviate the aggregation degree of the HTM and thus contributes to the quality of the film. After optimization of the concentration of HTMs (Fig. S8, ESI†), the M140-based device measured with a forward scan showed a PCE of 19.00% with an open circuit voltage (V_{OC}) of 1.11 V, a short-circuit current density (J_{SC}) of 23.13 mA cm^{-2}, and a fill factor (FF) of 0.74 under 1 sun illumination (AM 1.5G, 100 mW cm^{-2}) (Fig. 5b and Table 2). In contrast, the devices based on M141 achieved a better performance with a PCE of 20.74%, a V_{OC} of 1.13 V, an FF of 0.79, and a J_{SC} of 23.24 mA cm^{-2} (Fig. 5c).

It should be noted that devices based on both HTMs show negligible hysteresis, which can be attributed to the minimization of interfacial nonradiative recombination losses at the SnO_2 (with KCl treatment)/perovskite. The defect state passivation of perovskite with the K^+ cations and Cl^- anions resulted in a faster electron transfer from perovskite to SnO_2 and a slower recombination rate in the bulk perovskite film.[73] Also, the best J–V curves for the cells based on M130 and Spiro-OMeTAD (Fig. 5d) were collected and calculated to obtain the photovoltaic parameters as summarized in Table 2. The best efficiency of M141 is significantly improved compared with that of M130 (18.62%), hence confirming the positive influence of the MP-F-SFX triarylamine on HTM performances.

The performance statistics of PSCs are outlined in Fig. 5e; the average values for M140 and M141 are 18.63% and 20.28%, respectively (Table 2). The greatly improved PCE for M141 is mainly attributed to the highly enhanced FF and V_{OC} imparted by the change of the peripheral triarylamine, in which the incorporation of fluorene in MP-F-SFX resulted in a 2.3-fold higher hole mobility and 0.03 eV downshift of the HOMO (Table 1). Furthermore, to demonstrate the reliability of the device J–V curves, the

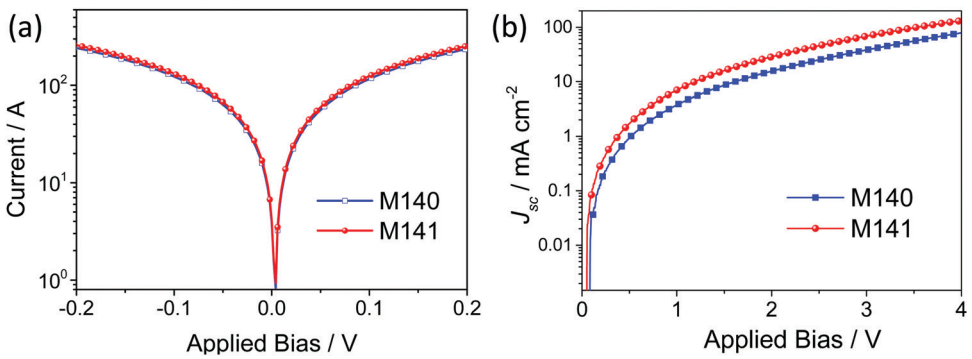

Fig. 4 (a) Conductivity and (b) hole mobility of doped M140 and M141.

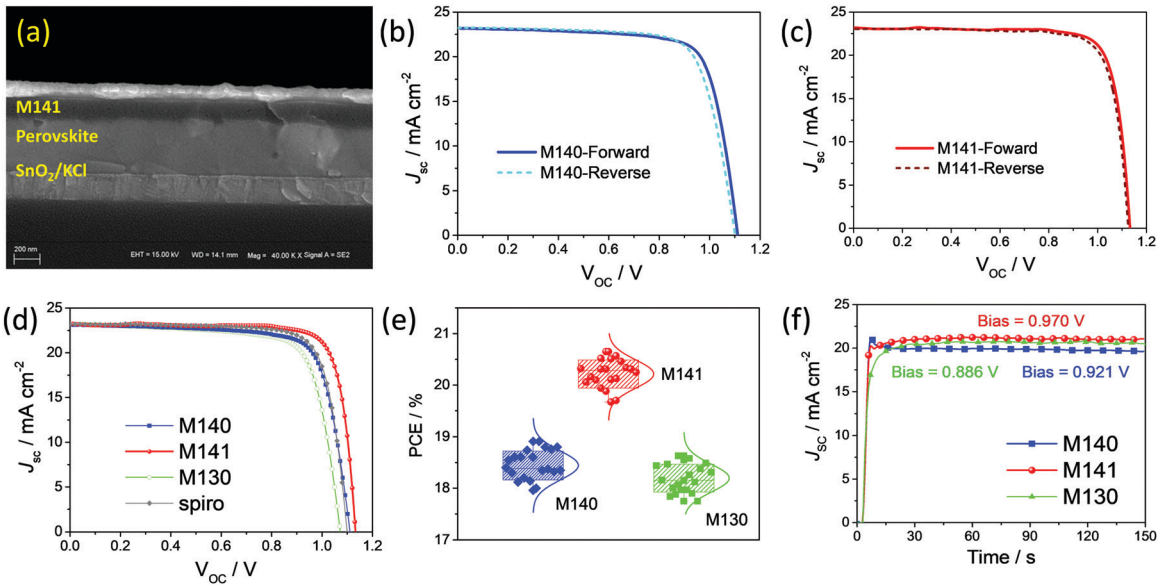

Fig. 5 (a) Cross-sectional SEM image of a PSC device with doped M141. Forward and reverse scanning *J*–*V* curves of PSCs based on doped M140 (b) and M141(c). (d) *J*–*V* curves of the optimized devices with different HTMs. (e) Statistical distribution of PSC performances with doped M140, M141 and M130. (f) Steady-state current densities of the PSCs based on doped M140, M141 and M130.

Table 2 Photovoltaic performances of PSCs under AM1.5G illumination (100 mW cm^{-2})

HTM	J_{SC}/mA cm^{-2}	V_{OC}/V	*FF*	Best PCE/%	Average PCE[a]/%
M140 (D)	23.13	1.11	0.74	19.00	18.63
M141 (D)	23.24	1.13	0.79	20.74	20.28
M130 (D)	23.20	1.07	0.75	18.62	18.20
Spiro[b] (D[c])	23.26	1.10	0.78	19.95	19.79
M140 (DF[d])	22.99	1.07	0.57	14.00	12.70
M141 (DF)	21.39	1.05	0.50	11.23	11.02

[a] The average PCE is obtained from 20 devices. [b] Spiro: abbreviation of Spiro-OMeTAD. [c] Doped HTMs. [d] Dopant-free HTMs.

stabilized current density was recorded at the maximum power point bias within 150 s for M140- and M141-based devices (Fig. 5f). M141 has a stable PCE output of 20.51% and a photocurrent of 21.15 mA cm^{-2}, while the stable PCE output is 18.27% and the photocurrent is 19.84 mA cm^{-2} for M140.

3.5. Surface morphologies of doped HTMs

The surface morphology of a doped HTM film is concerned with device parameters because a deteriorated morphology usually results in severe recombination and poor charge transport. The morphologies of the perovskite surface and HTM-coated perovskite films were analyzed by atomic force microscopy (AFM, Fig. 6a–c) and scanning electron microscopy (SEM, Fig. 6d and e). The AFM image of the bare perovskite film exhibits a uniform surface with a crystal size in the range of

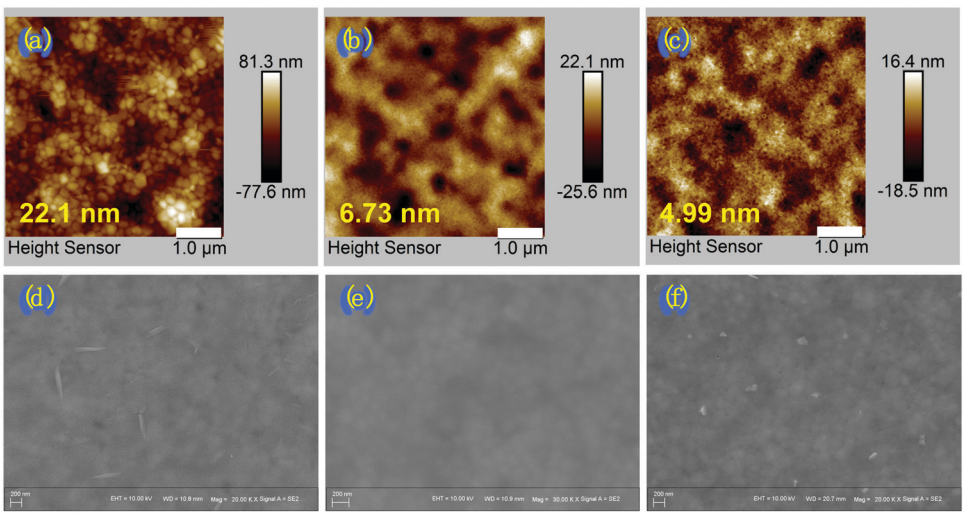

Fig. 6 AFM images (the scan size was 5 μm × 5 μm) of a bare perovskite film (a), and doped M140-coated (b) and M141-coated (c) perovskite films. SEM images of doped M140-coated (d), M141-coated (e) and M130-coated (f) perovskite films.

400–500 nm (Fig. 6a). M141 formed a uniform and pinhole-free film with the lowest root-mean-square (RMS) roughness value of 4.99 nm, verifying its excellent film-forming characteristics, which is in favor of increasing the interface interaction with perovskites and suppressing recombination. The RMS of the M140-coated film (6.73 nm) is larger than that of the M141-coated film (4.99 nm), which is caused by the enhanced crystallization tendency of M140 (see the next section). Similarly, the SEM image of M141 shows an extraordinarily homogeneous and smooth surface without any observable defects and particles (Fig. 6e). In contrast, some pinholes and particles existed in the M140 (Fig. 6d) and M130 counterparts (Fig. 6f).

To investigate the interactions between HTMs, the absorption of thin films based on M140, M141 and M130 was studied as shown in Fig. S9 (ESI†). In thin film form, the absorption spectrum of M140 shifts to a short wavelength by approximately 16 nm in comparison with its corresponding spectrum in solution, indicating H-aggregate formation in films. In contrast, the M130-based film exhibits a tiny shift of the absorption peak compared to that of solution. Therefore, the introduction of SFX in triarylamines leads to H-aggregates of HTMs. There are two reasons for the result. First, the spiro structure of SFX does not increase the intermolecular distance due to the nonplanar structure of the triarylamine. Second, the oxygen atom on the SFX may enhance the intermolecular interactions. Moreover, the M141-based film exhibits a small shift of the absorption peak (5 nm) compared to that of solution, although it has an SFX arm. Apparently, the outer arm of M141 results in a big 3D structure, which reduces the aggregates of HTMs.

3.6. Charge transport at the perovskite/HTM interface

Morphological analysis as discussed above implies that the interface contact for the doped M141-based device would be better than that of M140, which is intrinsically linked to the charge transport and charge recombination at the perovskite/HTM interface. The contribution of charge recombination/transport is further evaluated using the steady-state and time-resolved photoluminescence (PL and TRPL) spectra. As presented in Fig. 7a, the PL intensity in the central area of the perovskite is much higher than those of M140, M141 and M130, which indicates very efficient PL quenching for these HTMs. The quenching efficiency (*i.e.*, opposite to the PL intensity) decreases in the order of M141 (94.1%) > M140 (93.0%) > M130 (90.8%). Clearly, M141 bearing the MP-F-SFX donor bridge could quench the PL of the perovskite more efficiently than M140 and M130. The TRPL decay curves in Fig. 7b were fitted with the biexponential function $I(t) = A_1\exp(-t/\tau_1) + A_2\exp(-t/\tau_2)$, where τ_1 and τ_2 are the fast lifetime and long lifetime, respectively. We found that the perovskite films coated with M141 had a shorter τ_1 (2.21 ns) than the samples based on M140 (τ = 3.88 ns) and M130 (τ_1 = 3.63 ns). The results indicate an ultrahigh efficiency in the hole transfer process at the interface between the perovskite and M141, which finally contributes to the high FF value of the M141-based PSC.

Meanwhile, fast hole transfer could mitigate the negative effect of charge recombination. To compare the recombination kinetics of the devices based on different HTMs, the open-circuit voltage decay (OCVD) measurement was carried out. Fig. 7c shows the OCVD profiles of devices based on these HTMs. There is very fast voltage decay at the initial stage. After that, the electron recombination at the interface of SnO_2 and

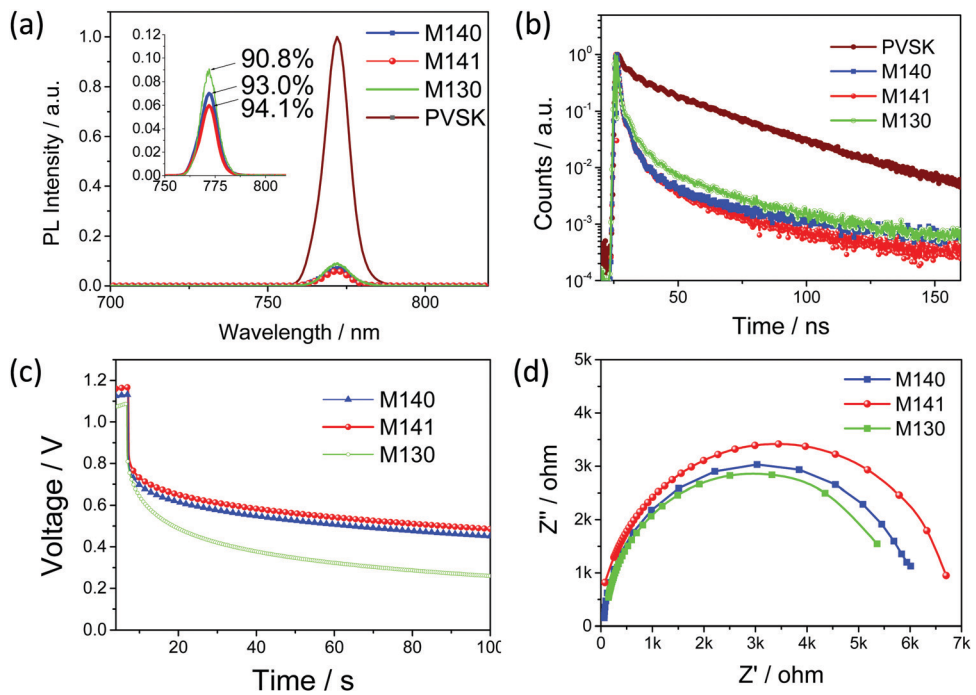

Fig. 7 (a) Steady-state PL spectra and (b) time-resolved PL decays of a bare perovskite film, and M140-, M141- and M130-coated perovskite films. (c) Open circuit voltage decay profiles and (b) Nyquist spectra of the studied PSCs.

the perovskite layer and HTMs starts to contribute to the voltage loss.[74] The slopes become steeper and steeper for devices based on M141, M140 and M130, indicating that the electron lifetimes are gradually enhanced with the increased bulk of the triarylamine donor.

Charge recombination behavior at the interfaces of PSCs was further investigated using electrochemical impedance spectra (EIS) of the corresponding PSCs in the dark at a potential bias of 0.9 V. The Nyquist plots in Fig. 7d show a semi-circle in the middle-frequency region, corresponding to the charge transport resistance (R_{ct}) at the perovskite/HTM interfaces. The M141-based device exhibits the largest R_{ct} (6914 Ω) value compared with the M140- (6046 Ω) and M130-based devices (5704 Ω), suggesting that M141 as a HTM can effectively reduce the charge recombination. The result is consistent with the results obtained from the OCVD measurements.

3.7. Device stability of doped devices

The operational stability of the devices in ambient air is in high demand for commercial application, which has a positive correlation with the HTM layer. Contact angle measurements of water droplets on the surfaces of doped M140, M141 and M130 are shown in Fig. 8a–c (the dopants used in the measurements are the same as in the photovoltaic devices). The M141-based film was hydrophobic with a water contact angle of 87.5°. In contrast, the M140- and M130-based films featuring two methoxy groups display lower water contact angles of 82.0° and 73.2°, respectively. The major contribution to the increased water contact observed for the M141-based film arises from its better high-quality film and decreased methoxy groups in the TAA. Therefore, the introduction of the MP-F-SFX triarylamine is beneficial for protection of the perovskite layer against degradation in the presence of moisture.

Operational stability data obtained with the device based on M141 are shown in Fig. 8d. The non-encapsulated device based on M141 was stored in ambient air with a humidity of about 30%. The device retains 80% of the initial PCE after storage for 1000 h, which is much better than the reference device based on Spiro-OMeTAD. The PCE of the Spiro-OMeTAD-based device rapidly decreases to around 62% of its initial value after 1000 h under the same conditions. Our analyses here suggest M141's ability to enable PSCs with high stability without sacrificing cell efficiency, a result that can be attributed to the high uniformity and enhanced hydrophobicity of the M141-based film.

3.8. Photovoltaic properties of dopant-free HTMs

To further investigate the influence of asymmetrical TAAs on the performance of HTMs, devices with dopant-free HTMs were fabricated. Fig. S10a (ESI†) presents a comparison of the best *J–V* curves of PSCs based on dopant-free M140 and M141. Unexpectedly, planar n–i–p structured PSCs based on dopant-free M140 achieve a PCE of 14.00% (Table 2), which is much better than that of M141 (PCE = 11.23%). The statistical distribution of dopant-free PSC performances (Fig. S10b, ESI†) further confirms this conclusion. The trend is contrary to the results based on doped devices. We further recorded the hole mobilities of dopant-free HTMs (Fig. S10c, ESI†). The hole mobility of additive-free M140 (2.25×10^{-6} cm^2 V^{-1} s^{-1}) is higher than that of

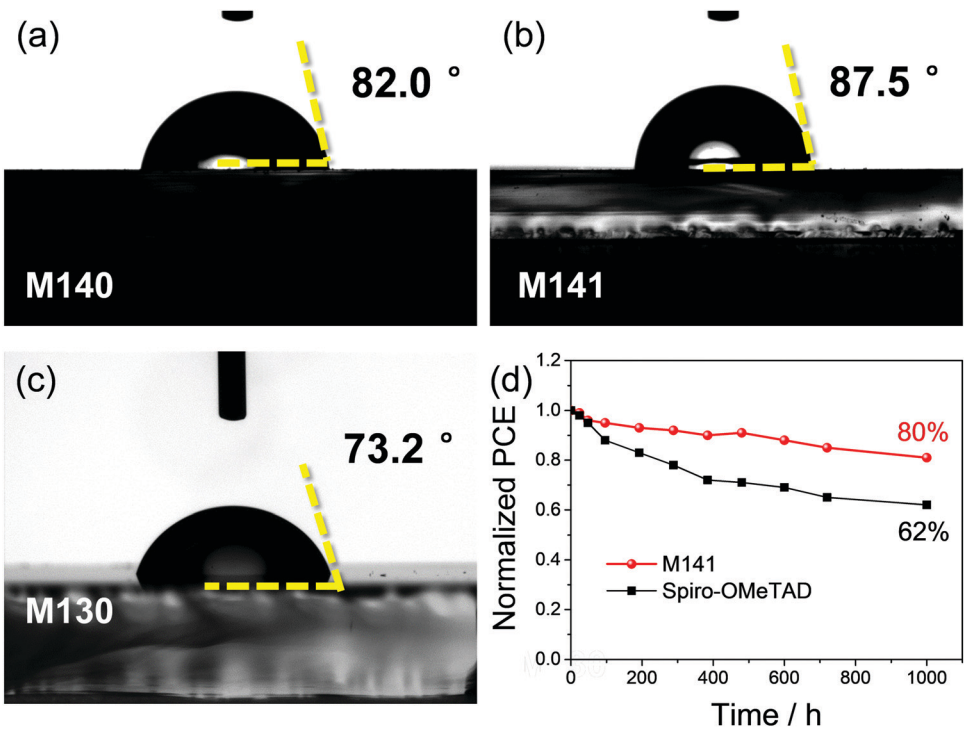

Fig. 8 The water contact angles of doped M140- (a), M141- (b), and M130-coated films (c) on ITO. (d) The normalized PCEs of PSCs based on M141 and Spiro-OMeTAD stored in ambient air with a humidity of about 30%.

M141 (1.35×10^{-6} cm^2 V^{-1} s^{-1}). It is well known that dopants such as LiTFSI and TBP are indispensable for Spiro-OMeTAD due to the orthogonal structure of spirofluorene and the propeller-like TPA.[16] M140 and M141, likewise, have bulky propeller-like TAA, which hinders the formation of close π–π stacking. However, MP-F-SFX in M141 is bigger than DMP-SFX in M140, leading to a decreased hole mobility of M141 when the dopants were removed. It should be noted that the PCEs of the dopant-free devices are much lower than those of the doped devices, suggesting that the M140 and M141 HTMs with bulky TAAs still rely on dopants. How to construct efficient dopant-free HTMs with bulky nonplanar TAAs is still a challenge.

4. Conclusions

In summary, we developed two new linear D–π–D HTMs based on asymmetrical TAA donors (DMP-SFX and MP-F-SFX). The arm modulation of the asymmetrical TAAs enables selective control of the energy level, hole mobility, film quality and thermal stability of linear D–π–D HTMs: (1) It is determined that the incorporation of highly conjugated SFX as the inside arm of the TAA makes it difficult for M140/M141 to oxidize, which, in turn, results in deep HOMO levels and thus enhanced V_{OC}s of devices. (2) The tendency of oriented aggregation (crystallization) of linear D–π–D HTMs, however, is governed by the outer arm of the TAA. Despite the perpendicular spiro structure, the inside SFX arm could not alleviate the HTM aggregation degree. (3) The promising donor MP-F-SFX exhibits the synergistic effects of its low-lying HOMO, improved hole mobility, high glass transition temperature and excellent film formability. Consequently, PSCs based on doped M141 provided an impressive PCE of 20.74% along with negligible hysteresis and good stability. We strongly believe that the design and synthesis of asymmetrical TAAs based on the synergistic strategy will drive the development of linear D–π–D HTMs toward robust higher performance PSCs.

Conflicts of interest

The authors declare that they have no known competing financial interests or personal relationships that could have appeared to influence the work reported in this paper.

Acknowledgements

We gratefully acknowledge the financial support from the National Natural Science Foundation of China (No. 22075210), the 111 Project (B12015), the Tianjin Natural Science Foundation (18JCYBJC21600, 18JCZDJC97000) and the Key University Science Research Project of Jiangsu Province (20KJA480001).

References

1 M. M. Lee, J. Teuscher, T. Miyasaka, T. N. Murakami and H. J. Snaith, Efficient Hybrid Solar Cells Based on Meso-Superstructured Organometal Halide Perovskites, *Science*, 2012, **338**, 643–647.

2 J. Peng, D. Walter, Y. Ren, M. Tebyetekerwa, Y. Wu, T. Duong, Q. Lin, J. Li, T. Lu, M. A. Mahmud, O. L. C. Lem, S. Zhao, W. Liu, Y. Liu, H. Shen, L. Li, F. Kremer, H. T. Nguyen, D.-Y. Choi, K. J. Weber, K. R. Catchpole and T. P. White, Nanoscale localized contacts for high fill factors in polymer-passivated perovskite solar cells, *Science*, 2021, **371**, 390–395.

3 M. A. R. Laskar, W. Luo, N. Ghimire, A. H. Chowdhury, B. Bahrami, A. Gurung, K. M. Reza, R. Pathak, R. S. Bobba, B. S. Lamsal, K. Chen, M. T. Rahman, S. I. Rahman, K. Emshadi, T. Xu, M. Liang, W.-H. Zhang and Q. Qiao, Phenylhydrazinium Iodide for Surface Passivation and Defects Suppression in Perovskite Solar Cells, *Adv. Funct. Mater.*, 2020, **30**, 2000778.

4 X. Liu, X. Zheng, Y. Wang, Z. Chen, F. Yao, Q. Zhang, G. Fang, Z.-K. Chen, W. Huang and Z.-X. Xu, Dopant-Free Hole-Transport Materials Based on Methoxytriphenylamine-Substituted Indacenodithienothiophene for Solution-Processed Perovskite Solar Cells, *ChemSusChem*, 2017, **10**, 2833–2838.

5 L. Tian, W. Zhang, Y. Huang, F. Wen, H. Yu, Y. Li, Q. Wang, C. Peng, Z. Ma, T. Hu, L. Du and M. Zhang, Effects of Annealing Time on Triple Cation Perovskite Films and Their Solar Cells, *ACS Appl. Mater. Interfaces*, 2020, **12**, 29344–29356.

6 L. Tian, F. Wen, W. Zhang, H. Zhang, H. Yu, P. Lin, X. Liu, S. Zhou, X. Zhou, Y. Jiang, T. Chen, Z. Ma, M. Zhang and Y. Huang, Rising from the Ashes: Gaseous Therapy for Robust and Large-Area Perovskite Solar Cells, *ACS Appl. Mater. Interfaces*, 2020, **12**, 49648–49658.

7 M. Jeong, I. W. Choi, E. M. Go, Y. Cho, M. Kim, B. Lee, S. Jeong, Y. Jo, H. W. Choi, J. Lee, J.-H. Bae, S. K. Kwak, D. S. Kim and C. Yang, Stable perovskite solar cells with efficiency exceeding 24.8% and 0.3-V voltage loss, *Science*, 2020, **369**, 1615–1620.

8 C. Chen, C. Wu, X. Ding, Y. Tian, M. Zheng, M. Cheng, H. Xu, Z. Jin and L. Ding, Constructing binary electron transport layer with cascade energy level alignment for efficient $CsPbI_2Br$ solar cells, *Nano Energy*, 2020, **71**, 104604.

9 X. Ding, H. Wang, C. Chen, H. Li, Y. Tian, Q. Li, C. Wu, L. Ding, X. Yang and M. Cheng, Passivation Functionalized Phenothiazine-Based Hole Transport Material for Highly Efficient Perovskite Solar Cell with Efficiency Exceeding 22%, *Chem. Eng. J.*, 2021, **410**, 128328.

10 G. Sathiyan, A. A. Syed, C. Chen, C. Wu, L. Tao, X. Ding, Y. Miao, G. Li, M. Cheng and L. Ding, Dual effective dopant based hole transport layer for stable and efficient perovskite solar cells, *Nano Energy*, 2020, **72**, 104673.

11 L. Liu, Y. Wu, M. Li, X. Zong, Z. Sun, M. Liang and S. Xue, Thieno[3,2-b]indole-based hole transporting materials for perovskite solar cells with photovoltages exceeding 1.11 V, *Chem. Commun.*, 2018, **54**, 14025–14028.

12 W. Hu, W. Zhou, X. Lei, P. Zhou, M. Zhang, T. Chen, H. Zeng, J. Zhu, S. Dai, S. Yang and S. Yang, Low-Temperature In Situ Amino Functionalization of TiO_2 Nanoparticles Sharpens Electron Management Achieving over 21% Efficient Planar Perovskite Solar Cells, *Adv. Mater.*, 2019, **31**, 1806095.

13 Q. Jiang, Z. Ni, G. Xu, Y. Lin, P. N. Rudd, R. Xue, Y. Li, Y. Li, Y. Gao and J. Huang, Interfacial Molecular Doping of Metal Halide Perovskites for Highly Efficient Solar Cells, *Adv. Mater.*, 2020, **32**, 2001581.

14 G.-W. Kim, H. Choi, M. Kim, J. Lee, S. Y. Son and T. Park, Hole Transport Materials in Conventional Structural (n–i–p) Perovskite Solar Cells: From Past to the Future, *Adv. Energy Mater.*, 2020, **10**, 1903403.

15 X. Yang, H. Wang, B. Cai, Z. Yu and L. Sun, Progress in hole-transporting materials for perovskite solar cells, *J. Energy Chem.*, 2018, **27**, 650–672.

16 X. Yin, Z. Song, Z. Li and W. Tang, Toward ideal hole transport materials: a review on recent progress in dopant-free hole transport materials for fabricating efficient and stable perovskite solar cells, *Energy Environ. Sci.*, 2020, **13**, 4057–4086.

17 X. Ding, C. Chen, L. Tao, C. Wu, M. Zheng, H. Lu, H. Xu, H. Li and M. Cheng, Dopant-free methoxy substituted copper(II) phthalocyanine for highly efficient and stable perovskite solar cells, *Chem. Eng. J.*, 2020, **387**, 124130.

18 Z. Li, X. Sun, Z. Li, X. Yu, X. Wu, C. Zhong, D. Liu, D. Lei, A. K. Y. Jen and Z. Zhu, Efficient Inverted Perovskite Solar Cells with Low Voltage Loss Achieved by a Pyridine-based Dopant-free Polymer Semiconductor, *Angew. Chem., Int. Ed.*, 2021, **60**, 7227–7233.

19 Y. Wang, Q. Liao, J. Chen, W. Huang, X. Zhuang, Y. Tang, B. Li, X. Yao, X. Feng, X. Zhang, M. Su, Z. He, T. J. Marks, A. Facchetti and X. Guo, Teaching an Old Anchoring Group New Tricks: Enabling Low-Cost, Eco-Friendly Hole-Transporting Materials for Efficient and Stable Perovskite Solar Cells, *J. Am. Chem. Soc.*, 2020, **142**, 16632–16643.

20 Y. Wang, W. Chen, L. Wang, B. Tu, T. Chen, B. Liu, K. Yang, C. W. Koh, X. Zhang, H. Sun, G. Chen, X. Feng, H. Y. Woo, A. B. Djurišić, Z. He and X. Guo, Dopant-Free Small-Molecule Hole-Transporting Material for Inverted Perovskite Solar Cells with Efficiency Exceeding 21%, *Adv. Mater.*, 2019, **31**, 1902781.

21 Y. Chen, X. Xu, N. Cai, S. Qian, R. Luo, Y. Huo and S.-W. Tsang, Rational Design of Dopant-Free Coplanar D-π-D Hole-Transporting Materials for High-Performance Perovskite Solar Cells with Fill Factor Exceeding 80%, *Adv. Energy Mater.*, 2019, **9**, 1901268.

22 K. Jiang, J. Wang, F. Wu, Q. Xue, Q. Yao, J. Zhang, Y. Chen, G. Zhang, Z. Zhu, H. Yan, L. Zhu and H.-L. Yip, Dopant-Free Organic Hole-Transporting Material for Efficient and Stable Inverted All-Inorganic and Hybrid Perovskite Solar Cells, *Adv. Mater.*, 2020, **32**, 1908011.

23 P. Xu, P. Liu, Y. Li, B. Xu, L. Kloo, L. Sun and Y. Hua, D–A–D-Typed Hole Transport Materials for Efficient Perovskite Solar Cells: Tuning Photovoltaic Properties via the Acceptor Group, *ACS Appl. Mater. Interfaces*, 2018, **10**, 19697–19703.

24 Y.-C. Chang, K.-M. Lee, C.-C. Ting and C.-Y. Liu, Step-efficient access to new starburst hole-transport materials with carbazole end-groups for perovskite solar cells via direct C–H/C–Br coupling reactions, *Mater. Chem. Front.*, 2019, **3**, 2041–2045.

25 X. Kong, Y. Jiang, X. Wu, C. Chen, J. Guo, S. Liu, X. Gao, G. Zhou, J.-M. Liu, K. Kempa and J. Gao, Dopant-free F-substituted benzodithiophene copolymer hole-transporting materials for efficient and stable perovskite solar cells, *J. Mater. Chem. A*, 2020, **8**, 1858–1864.

26 L. Zhang, X. Zhou, J. Xie, S. Chen, S. Bae, J. Kim and B. Xu, Conjugated polyelectrolyte with potassium cations enables inverted perovskite solar cells with an efficiency over 20%, *J. Mater. Chem. A*, 2020, **8**, 8238–8243.

27 X. Jiang, D. Wang, Z. Yu, W. Ma, H.-B. Li, X. Yang, F. Liu, A. Hagfeldt and L. Sun, Molecular Engineering of Copper Phthalocyanines: A Strategy in Developing Dopant-Free Hole-Transporting Materials for Efficient and Ambient-Stable Perovskite Solar Cells, *Adv. Energy Mater.*, 2019, **9**, 1803287.

28 Y. Feng, Q. Hu, E. Rezaee, M. Li, Z.-X. Xu, A. Lorenzoni, F. Mercuri and M. Muccini, High-Performance and Stable Perovskite Solar Cells Based on Dopant-Free Arylamine-Substituted Copper(II) Phthalocyanine Hole-Transporting Materials, *Adv. Energy Mater.*, 2019, **9**, 1901019.

29 Y.-K. Peng, K.-M. Lee, C.-C. Ting, M.-W. Hsu and C.-Y. Liu, Making benzotrithiophene derivatives dopant-free for perovskite solar cells: Step-saving installation of π-spacers by a direct C–H arylation strategy, *J. Mater. Chem. A*, 2019, **7**, 24765–24770.

30 Q.-Q. Ge, J.-Y. Shao, J. Ding, L.-Y. Deng, W.-K. Zhou, Y.-X. Chen, J.-Y. Ma, L.-J. Wan, J. Yao, J.-S. Hu and Y.-W. Zhong, A Two-Dimensional Hole-Transporting Material for High-Performance Perovskite Solar Cells with 20% Average Efficiency, *Angew. Chem., Int. Ed.*, 2018, **57**, 10959–10965.

31 C. Wu, C. Chen, L. Tao, X. Ding, M. Zheng, H. Li, G. Li, H. Lu and M. Cheng, Highly efficient perovskite solar cells based on symmetric hole transport material constructed with indaceno[1,2-b:5,6-b′]dithiophene core building block, *J. Energy Chem.*, 2020, **43**, 98–103.

32 P. Huang, Manju, S. Kazim, G. Sivakumar, M. Salado, R. Misra and S. Ahmad, Pyridine Bridging Diphenylamine-Carbazole with Linking Topology as Rational Hole Transporter for Perovskite Solar Cells Fabrication, *ACS Appl. Mater. Interfaces*, 2020, **12**, 22881–22890, DOI: 10.1021/acsami.0c03584.

33 K. Rakstys, S. Paek, A. Drevilkauskaite, H. Kanda, S. Daskeviciute, N. Shibayama, M. Daskeviciene, A. Gruodis, E. Kamarauskas, V. Jankauskas, V. Getautis and M. K. Nazeeruddin, Carbazole-Terminated Isomeric Hole-Transporting Materials for Perovskite Solar Cells, *ACS Appl. Mater. Interfaces*, 2020, **12**, 19710–19717.

34 L. Wan, W. Zhang, S. Fu, L. Chen, Y. Wang, Z. Xue, Y. Tao, W. Zhang, W. Song and J. Fang, Achieving over 21% efficiency in inverted perovskite solar cells by fluorinating a dopant-free hole transporting material, *J. Mater. Chem. A*, 2020, **8**, 6517–6523.

35 X. Zhou, F. Kong, Y. Sun, Y. Huang, X. Zhang and R. Ghadari, Benzothiadiazole-based hole transport materials for high-efficiency dopant-free perovskite solar cells: Molecular planarity effect, *J. Energy Chem.*, 2020, **44**, 115–120.

36 J. Wang, H. Zhang, B. Wu, Z. Wang, Z. Sun, S. Xue, Y. Wu, A. Hagfeldt and M. Liang, Indeno[1,2-b]carbazole as Methoxy-Free Donor Group: Constructing Efficient and

Stable Hole-Transporting Materials for Perovskite Solar Cells, *Angew. Chem., Int. Ed.*, 2019, **58**, 15721–15725.
37 S. Ma, X. Zhang, X. Liu, R. Ghadari, M. Cai, Y. Ding, M. Mateen and S. Dai, Pyridine-triphenylamine hole transport material for inverted perovskite solar cells, *J. Energy Chem.*, 2021, **54**, 395–402.
38 K. Guo, M. Wu, S. Yang, Z. Wang, J. Li, X. Liang, F. Zhang, Z. Liu and Z. Wang, Introduction of Fluorine Into spiro[fluorene-9,9′-xanthene]-Based Hole Transport Material to Obtain Sensitive-Dopant-Free, High Efficient and Stable Perovskite Solar Cells, *Sol. RRL*, 2019, **3**, 1800352.
39 J. Chen, J. Xia, W.-J. Gao, H.-J. Yu, J.-X. Zhong, C. Jia, Y.-S. Qin, Z. She, D.-B. Kuang and G. Shao, Tetraphenylbutadiene-Based Symmetric 3D Hole-Transporting Materials for Perovskite Solar Cells: A Trial Trade-off between Charge Mobility and Film Morphology, *ACS Appl. Mater. Interfaces*, 2020, **12**, 21088–21099.
40 B.-B. Cui, Y. Han, N. Yang, S. Yang, L. Zhang, Y. Wang, Y. Jia, L. Zhao, Y.-W. Zhong and Q. Chen, Propeller-shaped, Triarylamine-rich and Dopant-free Hole-Transporting Materials for Efficient n-i-p Perovskite Solar Cells, *ACS Appl. Mater. Interfaces*, 2018, **10**, 41592–41598.
41 W. Budiawan, K.-W. Lai, P. Karuppuswamy, T. S. Jadhav, Y.-A. Lu, K.-C. Ho, P.-C. Wang, C.-C. Chang and C.-W. Chu, Asymmetric Benzotrithiophene-Based Hole Transporting Materials Provide High-Efficiency Perovskite Solar Cells, *ACS Appl. Mater. Interfaces*, 2020, **12**, DOI: 10.1021/acsami.0c02204.
42 X.-D. Zhu, X.-J. Ma, Y.-K. Wang, Y. Li, C.-H. Gao, Z.-K. Wang, Z.-Q. Jiang and L.-S. Liao, Hole-Transporting Materials Incorporating Carbazole into Spiro-Core for Highly Efficient Perovskite Solar Cells, *Adv. Funct. Mater.*, 2019, **29**, 1807094.
43 L. Duan, Y. Chen, J. Jia, X. Zong, Z. Sun, Q. Wu and S. Xue, Dopant-Free Hole-Transport Materials Based on 2,4,6-Triarylpyridine for Inverted Planar Perovskite Solar Cells, *ACS Appl. Energy Mater.*, 2020, **3**, 1672–1683.
44 Y. Wu, Z. Wang, M. Liang, H. Cheng, M. Li, L. Liu, B. Wang, J. Wu, R. Prasad Ghimire, X. Wang, Z. Sun, S. Xue and Q. Qiao, Influence of Nonfused Cores on the Photovoltaic Performance of Linear Triphenylamine-Based Hole-Transporting Materials for Perovskite Solar Cells, *ACS Appl. Mater. Interfaces*, 2018, **10**, 17883–17895.
45 Y. Lu, X. Zong, Y. Wang, W. Zhang, Q. Wu, M. Liang and S. Xue, Noncovalent functionalization of hole-transport materials with multi-walled carbon nanotubes for stable inverted perovskite solar cells, *J. Mater. Chem. C*, 2019, **7**, 14306–14313.
46 M. Li, J. Wu, G. Wang, B. Wu, Z. Sun, S. Xue, Q. Qiao and M. Liang, The donor-dependent methoxy effects on the performance of hole-transporting materials for perovskite solar cells, *J. Energy Chem.*, 2020, **47**, 10–17.
47 H. D. Pham, S. M. Jain, M. Li, S. Manzhos, K. Feron, S. Pitchaimuthu, Z. Liu, N. Motta, H. Wang, J. R. Durrant and P. Sonar, Dopant-free novel hole-transporting materials based on quinacridone dye for high-performance and humidity-stable mesoporous perovskite solar cells, *J. Mater. Chem. A*, 2019, **7**, 5315–5323.
48 W.-J. Gao, H.-J. Yu, J. Chen, J. Xiao, J.-K. Fang, X.-R. Jia, C.-F. Peng, G. Shao and D.-B. Kuang, Simple hole-transporting materials containing twin-carbazole moiety and unconjugated flexible linker for efficient and stable perovskite solar cells, *Chem. Eng. J.*, 2021, **405**, 126434.
49 D. Zhang, T. Wu, P. Xu, Y. Ou, A. Sun, H. Ma, B. Cui, H. Sun, L. Ding and Y. Hua, Importance of terminated groups in 9,9-bis(4-methoxyphenyl)-substituted fluorene-based hole transport materials for highly efficient organic–inorganic hybrid and all-inorganic perovskite solar cells, *J. Mater. Chem. A*, 2019, **7**, 10319–10324.
50 S. Mabrouk, M. Zhang, Z. Wang, M. Liang, B. Bahrami, Y. Wu, J. Wu, Q. Qiao and S. Yang, Dithieno[3,2-b:2′,3′-d]pyrrole-based hole transport materials for perovskite solar cells with efficiencies over 18%, *J. Mater. Chem. A*, 2018, **6**, 7950–7958.
51 C. Lu, I. T. Choi, J. Kim and H. K. Kim, Simple synthesis and molecular engineering of low-cost and star-shaped carbazole-based hole transporting materials for highly efficient perovskite solar cells, *J. Mater. Chem. A*, 2017, **5**, 20263–20276.
52 V. A. Chiykowski, Y. Cao, H. Tan, D. P. Tabor, E. H. Sargent, A. Aspuru-Guzik and C. P. Berlinguette, Precise Control of Thermal and Redox Properties of Organic Hole-Transport Materials, *Angew. Chem., Int. Ed.*, 2018, **57**, 15529–15533.
53 H. Lu, B. He, Y. Ji, Y. Shan, C. Zhong, J. Xu, J. LiuYang, F. Wu and L. Zhu, Dopant-free hole transport materials processed with green solvent for efficient perovskite solar cells, *Chem. Eng. J.*, 2020, **385**, 123976.
54 Z. Yu, L. Wang, X. Mu, C.-C. Chen, Y. Wu, J. Cao and Y. Tang, Intramolecular Electric Field Construction in Metal Phthalocyanine as Dopant-Free Hole Transporting Material for Stable Perovskite Solar Cells with >21% Efficiency, *Angew. Chem., Int. Ed.*, 2021, **60**, 6294–6299, DOI: 10.1002/anie.202016087.
55 Y. Kim, G. Kim, N. J. Jeon, C. Lim, J. Seo and B. J. Kim, Methoxy-Functionalized Triarylamine-Based Hole-Transporting Polymers for Highly Efficient and Stable Perovskite Solar Cells, *ACS Energy Lett.*, 2020, **5**, 3304–3313.
56 D. Y. Lee, G. Sivakumar, Manju, R. Misra and S. I. Seok, Carbazole-Based Spiro[fluorene-9,9′-xanthene] as an Efficient Hole-Transporting Material for Perovskite Solar Cells, *ACS Appl. Mater. Interfaces*, 2020, **12**, 28246–28252, DOI: 10.1021/acsami.0c06318.
57 Y.-C. Chen, D.-Z. Lin, J.-C. Wang, J.-S. Ni, Y.-Y. Yu and C.-P. Chen, Facile star-shaped tetraphenylethylene-based molecules with fused ring-terminated diarylamine as interfacial hole transporting materials for inverted perovskite solar cells, *Mater. Chem. Front.*, 2021, **5**, 1373–1387, DOI: 10.1039/D0QM00728E.
58 Y. Ou, A. Sun, H. Li, T. Wu, D. Zhang, P. Xu, R. Zhao, L. Zhu, R. Wang, B. Xu, Y. Hua and L. Ding, Developing D–π–D hole-transport materials for perovskite solar cells: the effect of the π-bridge on device performance, *Mater. Chem. Front.*, 2021, **5**, 876–884.
59 M. Tepliakova, I. K. Yakushenko, E. I. Romadina, A. V. Novikov, P. M. Kuznetsov, K. J. Stevenson and P. A. Troshin, Strength of attraction: pyrene-based hole-transport materials

with effective π–π stacking for dopant-free perovskite solar cells, *Sustainable Energy Fuels*, 2021, **5**, 283–288.

60 J. Urieta-Mora, I. García-Benito, A. Molina-Ontoria and N. Martín, Hole transporting materials for perovskite solar cells: a chemical approach, *Chem. Soc. Rev.*, 2018, **47**, 8541–8571.

61 H. Guo, H. Zhang, C. Shen, D. Zhang, S. Liu, Y. Wu and W.-H. Zhu, A Coplanar π-Extended Quinoxaline Based Hole-Transporting Material Enabling over 21% Efficiency for Dopant-Free Perovskite Solar Cells, *Angew. Chem., Int. Ed.*, 2021, **60**, 2674–2679.

62 J. Zhou, X. Yin, Z. Dong, A. Ali, Z. Song, N. Shrestha, S. S. Bista, Q. Bao, R. J. Ellingson, Y. Yan and W. Tang, Dithieno[3,2-b:2′,3′-d]pyrrole Cored p-Type Semiconductors Enabling 20% Efficiency Dopant-Free Perovskite Solar Cells, *Angew. Chem., Int. Ed.*, 2019, **58**, 13717–13721.

63 T. Niu, W. Zhu, Y. Zhang, Q. Xue, X. Jiao, Z. Wang, Y.-M. Xie, P. Li, R. Chen, F. Huang, Y. Li, H.-L. Yip and Y. Cao, D-A-π-A-D-type Dopant-free Hole Transport Material for Low-Cost, Efficient, and Stable Perovskite Solar Cells, *Joule*, 2021, **5**, 249–269.

64 H. Zhu, Z. Shen, L. Pan, J. Han, F. T. Eickemeyer, Y. Ren, X. Li, S. Wang, H. Liu, X. Dong, S. M. Zakeeruddin, A. Hagfeldt, Y. Liu and M. Grätzel, Low-Cost Dopant Additive-Free Hole-Transporting Material for a Robust Perovskite Solar Cell with Efficiency Exceeding 21%, *ACS Energy Lett.*, 2021, **6**, 208–215.

65 B. X. Zhao, C. Yao, K. Gu, T. Liu, Y. Xia and Y.-L. Loo, A hole-transport material that also passivates perovskite surface defects for solar cells with improved efficiency and stability, *Energy Environ. Sci.*, 2020, **13**, 4334–4343.

66 N. J. Jeon, H. Na, E. H. Jung, T.-Y. Yang, Y. G. Lee, G. Kim, H.-W. Shin, S. Il Seok, J. Lee and J. Seo, A fluorene-terminated hole-transporting material for highly efficient and stable perovskite solar cells, *Nat. Energy*, 2018, **3**, 682–689.

67 X. Zhao, H.-S. Kim, J.-Y. Seo and N.-G. Park, Effect of Selective Contacts on the Thermal Stability of Perovskite Solar Cells, *ACS Appl. Mater. Interfaces*, 2017, **9**, 7148–7153.

68 B. Xu, J. Zhang, Y. Hua, P. Liu, L. Wang, C. Ruan, Y. Li, G. Boschloo, E. M. J. Johansson, L. Kloo, A. Hagfeldt, A. K. Y. Jen and L. Sun, Tailor-Making Low-Cost Spiro[fluorene-9,9′-xanthene]-Based 3D Oligomers for Perovskite Solar Cells, *Chem*, 2017, **2**, 676–687.

69 J. Zhang, B. Xu, L. Yang, C. Ruan, L. Wang, P. Liu, W. Zhang, N. Vlachopoulos, L. Kloo, G. Boschloo, L. Sun, A. Hagfeldt and E. M. J. Johansson, The Importance of Pendant Groups on Triphenylamine-Based Hole Transport Materials for Obtaining Perovskite Solar Cells with over 20% Efficiency, *Adv. Energy Mater.*, 2018, **8**, 1701209.

70 F. Liu, F. Wu, Z. Tu, Q. Liao, Y. Gong, L. Zhu, Q. Li and Z. Li, Hole Transport Materials Based on 6,12-Dihydroindeno[1,2-b]fluorine with Different Periphery Groups: A New Strategy for Dopant-Free Perovskite Solar Cells, *Adv. Funct. Mater.*, 2019, **29**, 1901296.

71 J. Cao, F. Du, L. Yang and W. Tang, The design of dithieno[3,2-b:2′,3′-d]pyrrole organic photovoltaic materials for high-efficiency organic/perovskite solar cells, *J. Mater. Chem. A*, 2020, **8**, 22572–22592.

72 F. Liu, F. Wu, W. Ling, Z. Tu, J. Zhang, Z. Wei, L. Zhu, Q. Li and Z. Li, Facile-Effective Hole-Transporting Materials Based on Dibenzo[a,c]carbazole: The Key Role of Linkage Position to Photovoltaic Performance of Perovskite Solar Cells, *ACS Energy Lett.*, 2019, **4**, 2514–2521.

73 F. Li, Z. Shen, Y. Weng, Q. Lou, C. Chen, L. Shen, W. Guo and G. Li, Novel Electron Transport Layer Material for Perovskite Solar Cells with Over 22% Efficiency and Long-Term Stability, *Adv. Funct. Mater.*, 2020, **30**, 2004933.

74 Q. Wang, Fast Voltage Decay in Perovskite Solar Cells Caused by Depolarization of Perovskite Layer, *J. Phys. Chem. C*, 2018, **122**, 4822–4827.

